# NUMERICAL COMPUTATIONS OF TURBULENT FLOW THROUGH ORIFICE FLOW METER

**Aleksandar S. Ćoćić, Milan M. Raković, Ilić B. Dejan, Milan R. Lečić**

University of Belgrade, Faculty of Mechanical Engineering, Kraljice Marije 16, 11120 Belgrade 35
e-mail: acocic@mas.bg.ac.rs, milan.rakovic992@gmail.com, dilic@mas.bg.ac.rs, mlecic@mas.bg.ac.rs

**Abstract.** Turbulent, incompressible flow through orifice flow meter is numerically investigated using OpenFOAM software. Turbulence is modeled using RANS approach, and three turbulence models are tested: standard $k$-$\varepsilon$, $k-\omega$ and Launder Sharma model. Results for pressure drop on the orifice are compared to experimental results and good agreement is found for all turbulent models, with the most accurate results obtained with $k-\varepsilon$ model. Velocity and pressure distribution in whole computational domain is analyzed, with special attention to the region in proximity to the orifice where primary and secondary vortex structures are detected. Additionally, numerical computations are also performed on automatically generated mesh using snappyHexMesh utility and similar results for the pressure drop are obtained as the ones on the block-structured grid.

## 1. Introduction

Orifice flow meters are very common devices for flow rate measurements in various industry applications. Their widespread usage is due to several advantages like robustness, simplicity in construction and installation. Additionally, they don't have any moving parts, and they can be used with any kind of fluids. Orifice flow meters works on simple principle which is based on velocity and pressure variation caused by reduction of flow area. Flow rate is determined by measuring the pressure difference caused by the orifice flow meter and using simple algebraic equation. However, in that equation there is one parameter which has to be determined experimentally and that is discharge coefficient $C_d$. It represents the ratio of the actual flow and theoretical flow. In that sense, each flow meter is supplied with installation procedure and values of discharge coefficient. In international trade, it is implemented in accordance with international standard ISO 5167-1. In determination of discharge coefficient, experiments have to be conducted in controlled conditions of fully developed, purely axial flow without swirl upstream of the orifice. Downstream of the orifice definite straight segment of the pipe has to be installed, in order to avoid the effects of outlet conditions to the flow structure downstream the orifice. Qualitative and quantitative understanding of the flow structure through orifice flow meter can be very useful tool for more accurate and sensitive flow measurement using that device. Advanced experimental techniques like Particle Image Velocimety (PIV) can be used for that purpose, but that task can be also fulfilled using Computational Fluid Dynamics (CFD).

There are not so many published results of numerical simulations of flow patterns for the orifice. Durst and Wang [1] use $k-\varepsilon$ model for numerical calculations of the flow in circular pipe with sudden area contraction. They found good agreement with experimental data for axial and radial velocities, but

data about pressure drop was not reported. Ćoćić et al. [2] analyzed the same problem as in [1] using invariant theory and numerical simulations. Authors used detailed experimental data of Durst and Wang available at ERCOFTAC Classical Database [3]. Analysis of experimental data for turbulent stresses in Anisotropy Invariant Map (AIM) introduced by Lumley and Newman [4] showed that experimental data in wall region should be rejected since they describes physically impossible states of turbulence. Numerical simulations were performed using OpenFOAM-1.3 software and several turbulence models. Authors used standard $k-\varepsilon$, RNG $k-\varepsilon$ and Launder-Gibson RSM (high-Re) and Launder-Sharma (low-Re) turbulence models. They found that all models give similar predictions in terms of mean velocities while Launder-Sharma model gives the best agreement with experimental data, especially in comparison of turbulence quantities. Smith et al. [5] studied the effect of orifice-to-pipe diameter ratio from 0.5 to 0.8 on the flow field using $k-\varepsilon$ and RSM turbulence model. Roul and Sukanta [6] analyzed single-phased and two-phased flow through thin and thick orifices using CFD and Eulerian-Eulerian model. The results obtained from numerical simulations are validated against experimental data from the literature and good agreement is found. Manish et al. [7] performed numerical simulation using $k-\varepsilon$ model and OpenFOAM-1.6 solver and validated the results with the previously published experimental data by other researches. They propose a new scheme to track vena-contracta with the help of CFD. Nygård and Andersson investigate turbulent flow through an abrupt axisymmetric contraction by solving full three-dimensional Navier-Stokes in cylindrical coordinates. They model the orifice using immersed boundary method and compare obtained results with experimental data in the separated-flow region downstream of the obstruction.

In this paper, the flow through orifice flow meter installed in Laboratory for Hydraulic Machinery at Faculty of Mechanical Engineering in Belgrade is numerically investigated using OpenFOAM software [9]. Performances of several turbulence model are tested. Two approaches have been used for mesh generation: block structured grid using blockMesh and hexa-dominant unstructured grid using snappyHexMesh application available within OpenFOAM. Comparison of results and convergence criteria is performed on these two types of grid. Additionally, prior to numerical simulation, experiments were performed where pressure drop is measured for various values of flow rate.

## 2. Experimental rig and computational domain

Experimental rig at which orifice flow meter considered in this paper is installed is shown in Figure 1. Water is used as a working fluid and flow rate is measured with three different measuring methods (devices): volumetric method, ultrasonic flow meter and orifice flow meter. Last two measuring devices are installed in steel pipe of inner diameter $D = 165\,\text{mm}$, and characteristical pipe lengths are $L_1 = 2\,\text{m}$ and $L_2 = 6\,\text{m}$. On this experimental rig it is assured that fully developed axial flow is present in both cross-sections before the ultrasonic and orifice flow meter. Experiments were performed for four different pump regimes, with four different rotational speed of pump impeller. The volume flow rate is simultaneously measured on three devices for all regimes. In volumetric method time and volume in calibrated reservoir, designated with 10 in Figure 1, is measured, on ultrasonic meter flow is read from display, while on orifice flow meter the pressure drop is measured using differential U-tube manometer.

Based on measured pressure drop, volume flow rate can be determined using the expression

$$Q = C_d A_0 \sqrt{\frac{2(p_1 - p_2)}{\rho(1-\beta^4)}} = C_d A_0 \sqrt{\frac{2\Delta p}{\rho(1-\beta^4)}} \tag{1}$$

where $C_d$ is discharge coefficient of orifice flow meter, $A_0$ is flow area, $\Delta p$ is the pressure drop and $\beta$ is diameter ratio, $\beta = d_u/D$.

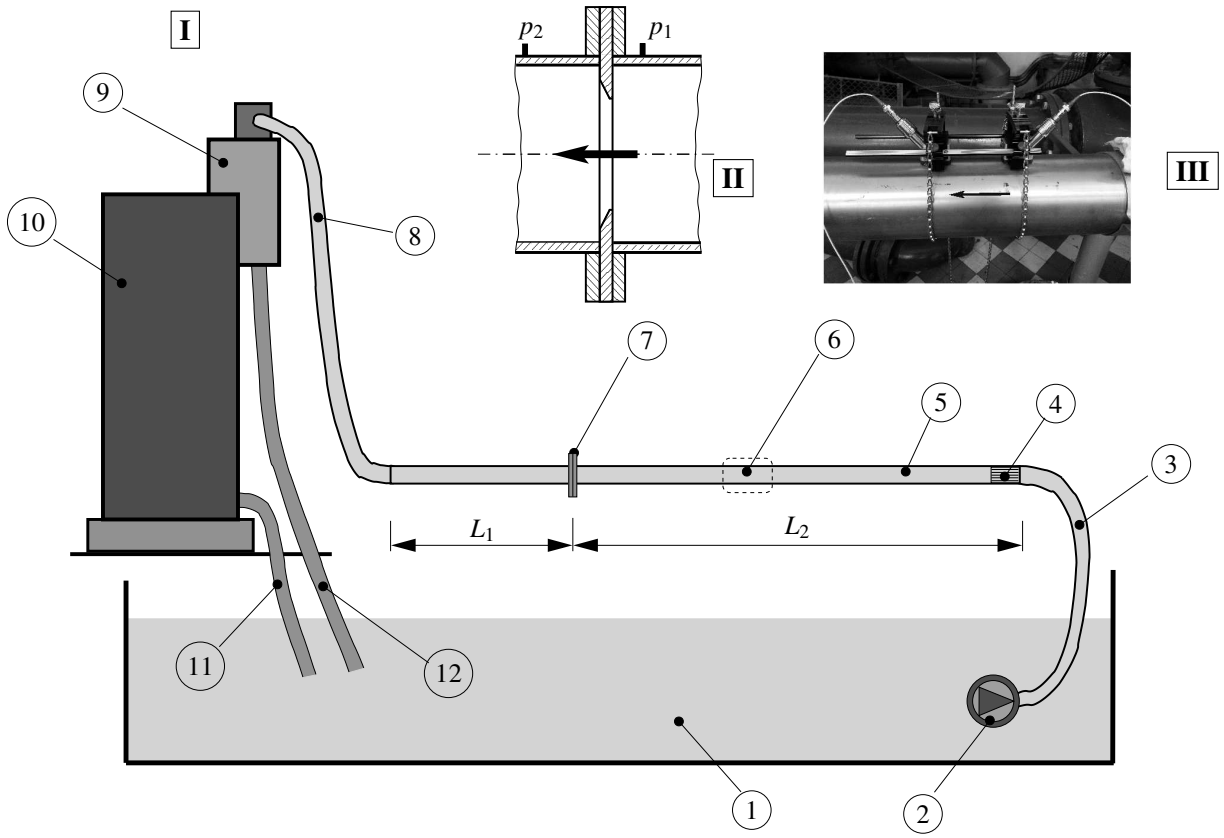


**Figure 1.** Experimental rig for volume flow measurements: 1 - reservoir, 2 - centrifugal pump, 3 - flexible hose, 4 - flow straightener, 5 - steel pipe, 6 - ultrasonic flow meter, 7 - orifice flow meter, 8 - flexible hose, 9 - diverter, 10 - calibrating reservoir, 11 and 12 - flexible hose; **I** - volumetric method for flow rate measurement, **II** - flow rate measurement with orifice flow meter, **III** - flow rate measurement with ultrasonic method.

| Regime | 1 | 2 | 3 | 4 |
|---|---|---|---|---|
| $Q_{\text{vm}}\,[\text{lit/s}]$ | 7.4938 | 10.2721 | 12.5075 | 14.1620 |
| $Q_{\text{us}}\,[\text{lit/s}]$ | 7.5 | 10.3 | 12.3 | 14.2 |
| $Q_{\text{or}}\,[\text{lit/s}]$ | 7.5011 | 10.5274 | 12.5081 | 14.2943 |
| $\Delta p\,[\text{kPa}]$ | 1.5686 | 3.0393 | 4.4118 | 5.6863 |

**Table 1.** Experimental values of flow rate and pressure drop on orifice flow meter: $Q_{\text{vm}}$ - flow rate measured with volumetric method, $Q_{\text{us}}$ - flow rate measured with ultrasonic meter; $Q_{\text{or}}$ - flow rate calculated using calibration formula of orifice flow meter.

The results for four different regimes are given in Table 1. It can be seen that nearly identical values of volume flow rate is obtained using all three measuring methods. These experimental data will be used as a validation tool for numerical computations. In these computations, volume flow rate through computational domain will be varied, and the pressure drop on the orifice meter will be determined and compared with experimental results. Additionally, flow structure inside the computational domain will be also analyzed. This computational domain is the part of experimental rig, and together with characteristical orifice dimensions is shown in Figure 2.

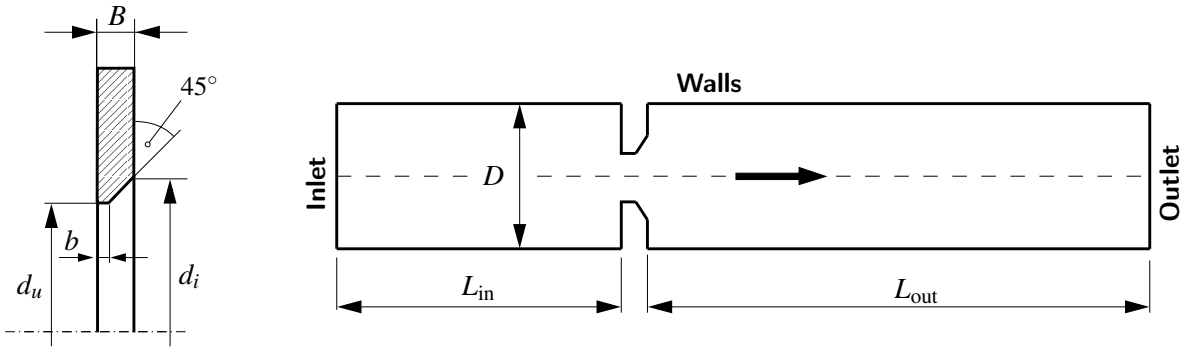


**Figure 2.** Dimensions of orifice meter and domain for numerical computations: $B = 10.7\,\text{mm}$, $b = 2\,\text{mm}$, $d_u = 90\,\text{mm}$, $d_i = 107.4\,\text{mm}$, $D = 165\,\text{mm}$, $L_{\text{in}} = 1\,\text{m}$, $L_{\text{out}} = 4\,\text{m}$.

## 3. Governing equations

Reynolds averaged Navier-Stokes (RANS) approach is used for mathematical description of the flow. It is assumed that the flow is incompressible and statistically steady, so the RANS equations, together with Boussinesq eddy viscosity assumption are:

$$\nabla \cdot \vec{U} = 0, \tag{2}$$

$$\nabla \cdot (\vec{U} \otimes \vec{U}) = -\nabla P + (\nu + \nu_t)\nabla^2 \vec{U}, \tag{3}$$

where $\vec{U}$ is time averaged velocity vector, $P$ is time averaged kinematic pressure, $\nu$ is kinematic viscosity of the fluid and $\nu_t$ is eddy or turbulent viscosity. In contrast to kinematic viscosity, which is the fluid property, turbulent viscosity is the property of the flow, and it is determined from additional, auxiliary equations. In most cases, they are two partial differential equations. Determination of auxiliary equations is the one of the main topic in area of turbulence modeling. These auxiliary equations used for determination of eddy viscosity are not universal, and it is quite certain that their universality is not possible since the Boussinesq assumption is not suitable for all types of turbulent flows. However, in most of cases where turbulence anisotropy is not pronounced this assumption give reasonably accurate results.

One of the most widely used turbulence model is $k-\varepsilon$ model which proved as the most robust in terms of numerical calculations, and in most cases, quite acceptable in terms of accuracy. Turbulent viscosity is calculated using the values of turbulent kinetic energy $k$ and its dissipation $\varepsilon$ using the expression

$$\nu_t = C_\mu \frac{k^2}{\varepsilon}, \tag{4}$$

where $C_\mu = 0.09$ is constant. Prior to calculation of $\nu_t$ using this expression, values of $k$ and $\varepsilon$ are determined from their transport equations. Original formulation of the model is given by Jones and Launder [10], and starting from this original model, many variants of $k-\varepsilon$ model is derived. One of them is Launder-Sharma model [11], which in contrast to original or standard $k-\varepsilon$ model doesn't use wall functions, but calculates the flow in viscous sub-layer. From numerical point of view, usage of this model requires the value $y^+ < 1$, i.e. very fine grid resolution near the wall surfaces. Problems of near wall behaviour $\varepsilon$ is improved with $k-\omega$ model, originally formulated by Wilcox [12], where $\omega$ is specific dissipation rate, while eddy viscosity is calculated using the expression

$$\nu_t = \frac{k}{\omega} \tag{5}$$

In this paper, these three aforementioned turbulence models are used for the computations and obtained results are compared and analyzed.

## 4. Numerical grid and numerical set-up in OpenFOAM

Generation of numerical grid for computational domain shown in Figure 2 is performed using two different approaches. By subdividing the domain to hexahedra blocks, block-structured grid is created using blockMesh utility (mesh M1), and in second approach a numerical grid is created with automated algorithm starting from triangulated surface geometries in Stereolithography (STL) format (mesh M2). For that purpose snappyHexMesh utility has been used. In this automated algorithm mesh conforms to the surface by iteratively refining a starting mesh and morphing the resulting split-hex mesh to the surface, with an optional phase with shrinking back the resulting mesh and inserting cell layers, [13]. Final mesh contains hexahedra and split-hexadra cells. These phases in mesh generation processes with snappyHexMesh utility are shown in Figure 3.

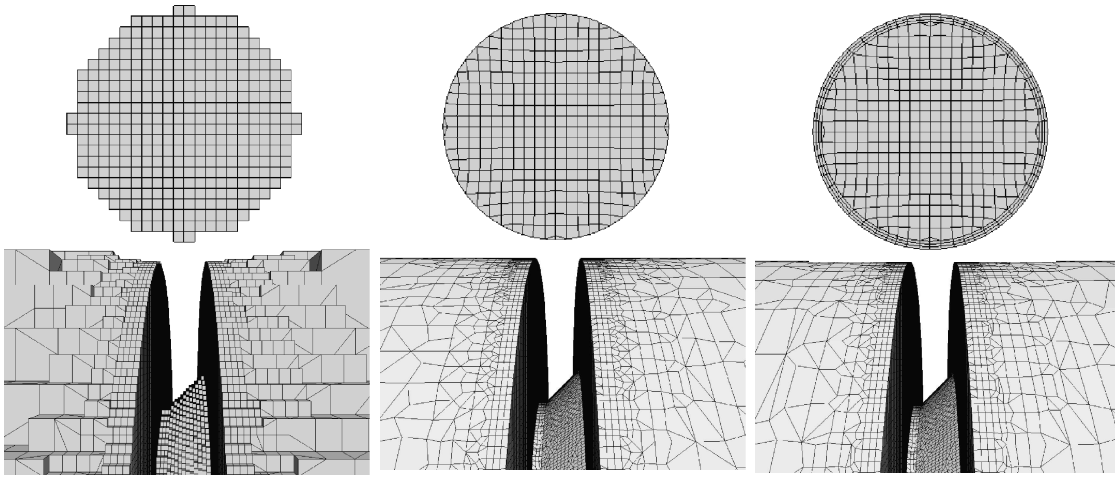

**Figure 3.** Three distinctive processes in mesh generation with snappyHexMesh utility at the inlet surface: castellation, snapping and adding layers.

Detailed explanation of both approaches for mesh generation can be found in [14].

### *4.1. Boundary conditions, discretization schemes and linear solvers*

For all cases, the same boundary conditions are used on inlet and outlet surfaces for all physical quantities. At the inlet surface, so called mapped boundary condition for velocity and turbulence quantities is used. This boundary condition maps the values of physical quantities from predefined cross-section inside the domain back to inlet surface. The distance from inlet to mapping surface is taken to be $L_m = 5D$, and additionally the values of mean velocity based on measured flow rate, and turbulence quantities is prescribed. This boundary condition enables profiles of fully developed flow at the inlet with predefined mean values, and drastically reduce the length of the domain before the orifice, and in the same time the number of cells. For (kinematic) pressure, zero gradient is defined at the inlet surface, while at the outlet fixed value $p = 0\,\mathrm{m}^2/\mathrm{s}^2$ is defined. For velocity and turbulence quantities, zero gradient boundary condition is defined at the outlet surface. At wall surfaces, wall functions are used for $k-\varepsilon$ and $k-\omega$ model, while for low-Re Launder-Sharma model the value of $10^{-10}\,\mathrm{m}^2/\mathrm{s}^2$ is set for turbulence kinetic energy $k$ and zero gradient for turbulent dissipation $\varepsilon$.

Second order upwind scheme [15] is used for discretization of convective term in equation (3), while for convective terms in transport equations for turbulence quantities limited linear scheme is used. For gradient and diffusion terms central differencing scheme is used. For solution of RANS equations (2), (3) characteristic thing is that there is no independent equation for pressure, whose gradients contribute to each of three momentum equations, [16]. These difficulties are overcomed using numerical procedure called SIMPLE algorithm [17]. Generalised geometric algebraic multigrid (GAMG) linear solver is used as matrix solver for pressure, while conjugate gradient solver with Gauss-Seidel smoother is used for all other quantities. Values of under-relaxation factors for pressure, velocity and turbulence quantities are 0.3, 0.7 and 0.5, respectively.

Kinematic viscosity of the water is taken to be $\nu = 1.06705 \cdot 10^{-6}\,\mathrm{m}^2/\mathrm{s}$, which is the value for working temperature $t = 18\,^{\circ}\mathrm{C}$.

## 5. Results and discussion

Grid independence test is performed for both numerical meshes mentioned in previous sections, by monitoring pressure drop, but also by comparing the velocity profiles in two cross-sections, in one before and in other after the orifice. The results presented here are related to meshes with 200000 cells (mesh M1) and 250000 cells (mesh M2). In mesh generation process for mesh M2 the intention was to get the number of cells close to number of cells of mesh M1.

### *5.1. Comparison of results for different turbulence models*

Performance of different turbulence models is tested for mesh M1. For usage of Launder-Sharma model it was necessary to make modification of the mesh, in order to assure $y^+ < 1$. This modified mesh M1 has 700000 cells. This large number of cells is consequence of very fine cell resolution near the wall, but also the fact that special care is taken to avoid the high aspect ratio of neighbouring cells. For $k-\varepsilon$ and $k-\omega$ model the same mesh was used, with previously mention 200000 cells, where it was assured that $y^+ \approx 30$. The results for pressure drop for all models are shown in Table 2, together with relative error in percentages.

| Experiment | | | $k-\varepsilon$ | | $k-\omega$ | | Launder Sharma | |
|---|---|---|---|---|---|---|---|---|
| Regime | $Q$ [lit/s] | $\Delta p$ kPa | $\Delta p$ [kPa] | $E$[%] | $\Delta p$ [kPa] | $E$[%] | $\Delta p$ [kPa] | $E$[%] |
| 1 | 7.4938 | 1.5686 | 1.559 | 0.615 | 1.597 | -1.807 | 1.5741 | -0.347 |
| 2 | 10.2721 | 3.0393 | 2.975 | 2.114 | 3.008 | 1.028 | 2.9271 | 3.670 |
| 3 | 12.5075 | 4.4118 | 4.405 | 0.155 | 4.465 | -1.205 | 4.350 | 1.401 |
| 4 | 14.1620 | 5.6863 | 5.632 | 0.740 | 5.723 | -0.864 | 5.566 | 1.903 |

**Table 2.** Numerical results for pressure drop obtained with three turbulence models.

It is evident that $k-\varepsilon$ model has the best overall performance. It can be also concluded that computations of viscous sub-layer in Launder Sharma model doesn't contribute to more accurate solution for pressure drop in comparison to $k$-$\varepsilon$ model, and that models with wall functions. On the other hand, computational cost is much higher, so further investigations are performed using only $k$-$\varepsilon$ model, and all following results are obtained using that model.

### *5.2. Comparison of results obtained with k-ε model on numerical meshes M1 and M2*

Results for pressure drop for four different regimes obtained on numerical mesh created with snappyHexMesh utility (M2), together with results for block-structured grid (M1) are given in Table 3.

| Experiment | | | Mesh M1 | | Mesh M2 | |
|---|---|---|---|---|---|---|
| Regime | $Q$ [lit/s] | $\Delta p$ kPa | $\Delta p$ [kPa] | $E$[%] | $\Delta p$ [kPa] | $E$[%] |
| 1 | 7.4938 | 1.5686 | 1.559 | 0.615 | 1.6123 | -2.783 |
| 2 | 10.2721 | 3.0393 | 2.975 | 2.114 | 3.027 | 0.403 |
| 3 | 12.5075 | 4.4118 | 4.405 | 0.155 | 4.451 | 0.888 |
| 4 | 14.1620 | 5.6863 | 5.632 | 0.740 | 5.685 | 0.024 |

**Table 3.** Results for pressure drop for numerical meshes M1 and M2, obtained with $k$-$\varepsilon$ model.

It is evident that results for mesh M2 have also quite good accuracy - overall, quite similar to results for mesh M1. Slight differences in the results are consequence of different cells distribution in the mesh. With block-structured definition of numerical mesh it is possible to have excellent control of cell sizes and their distribution in whole computational domain, especially near the solid boundaries. On the other hand, this method of mesh generation is time consuming, and for more complex geometries practically impossible. In that cases, automated mesh generation with snappyHexMesh is the only practical solution. Our investigation on this particular case shown that overall accuracy of numerical computations on that kind of numerical meshes is quite high. Additionally, there are no instabilities in iterative processes during numerical solutions, and residual values of all quantities smoothly converged to prescribed values of $10^{-6}$.

### *5.3. Flow patterns, pressure and velocity distribution inside the computational domain for third flow regime*

Contrary to experimental research, where some global parameter is measured (like flow rate), or physical quantities in particular points, or some small region in domain, CFD computations give the distribution of physical quantities in whole domain. With advanced postprocessing methods it's possible to detect coherent flow structures in the domain.

Flow pattern in orifice region in one axi-symmetric plane is shown in Figure 4.

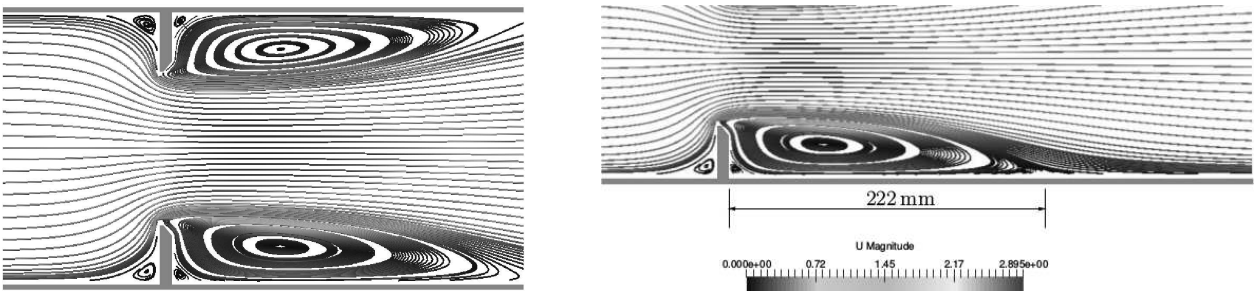


**Figure 4.** Streamlines of mean (time averaged) velocity in orifice region.

Four distinctive vortex regions are noticed in this plane. Besides large vortex structure due to sudden expansion of the cross-section after the orifice, two secondary vortices in regions near the pipe wall are present. The reason for appearance of these vortices are inability of the fluid to adjust instantly to sudden changes in geometry. After the orifice, this secondary vortex receives mass and momentum from the primary vortex, causing it to rotate counter to the primary vortex. Momentum transfer is due to viscous forces, turbulent mixing and mass transfer across the primary-secondary vortex interface. Computations shown that flow regime reattachment length of primary vortex is 222 mm. This value is obtained from the condition of zero wall shear stress at the pipe wall.

Velocity and pressure distribution along the pipe axis is given in Figure 5. High gradients of velocity and pressure are clearly visible at axial position of the orifice. Due to the sudden decrease in flow area, velocity is increasing (positive gradient in axial direction), while the pressure is decreasing (negative gradient). After the orifice, since the flow area is increasing we have opposite trends in comparison to the behaviour at the orifice, for both pressure and axial velocity. Here it also important to note that diagram shown in Figure 5 shows negative values of pressure. That is, of course, physically impossible, since the lowest value of pressure is 0 Pa, which is vacuum. This pressure is relative pressure, measured from the reference pressure value which is specified at the outlet. How flow considered here is incompressible, the value of pressure itself is not that important, but the pressure difference. In that sense, it is custom to set the value $P = p/\rho = 0\,\mathrm{m}^2/\mathrm{s}^2$ at the outlet of the computational domain. Minimal value of this pressure difference calculated in respect to the pressure at the outlet is $\Delta p = -1.05047\,\mathrm{kPa}$, and it's locate at position of velocity maximum, which is $U_{\max} = 2.89708\,\mathrm{m/s}$.

Evolution of axial velocity profile in axial direction after the orifice is shown in Figure 6. First cross-section shown, at distance of $x = 4.3\,\mathrm{mm}$ corresponds to center of secondary vortices which is formed in the corner of orifice and pipe wall (visually shown in Figure 4). Mean axial velocity in this

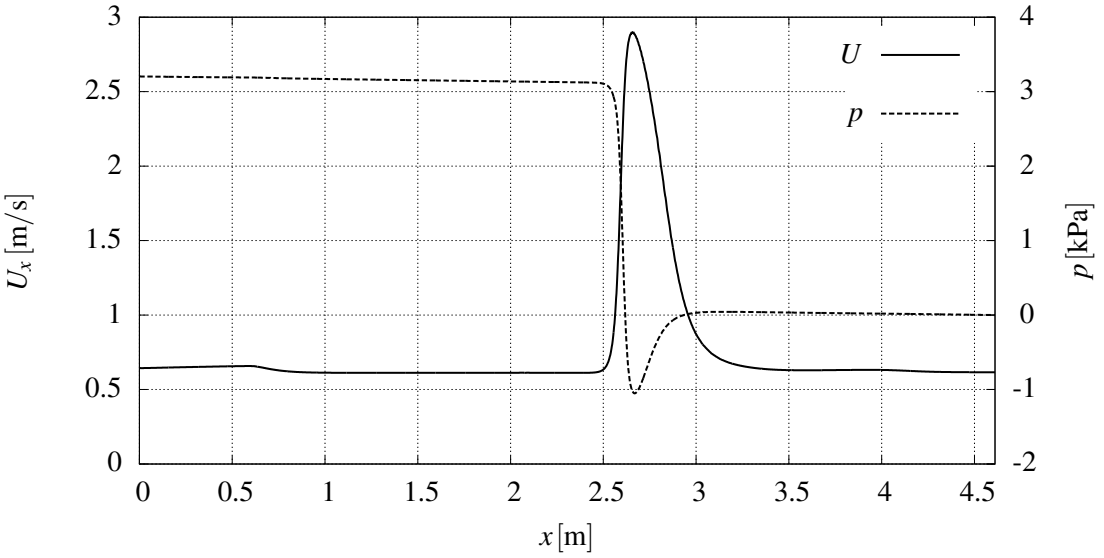


**Figure 5.** Distribution of pressure and velocity along the pipe axis.

region is very close to zero, which means that mean kinetic energy of this vortex is much smaller in comparison to primary vortex. One cross-section in primary vortex is shown in second diagram, which is at distance of $x = 66.3\,\text{mm}$. Here we can see much highly pronounced reversed flow near the pipe wall. Cross-section $x = 222\,\text{mm}$ represents the section where the shear layer reattaches to the pipe wall. In further cross-section axial velocity profile is transforming to velocity profile which corresponds to the fully developed turbulent profile of mean axial velocity. After the distance of $x = 1689.3\,\text{mm}$ there are no further changes of profile in axial direction.

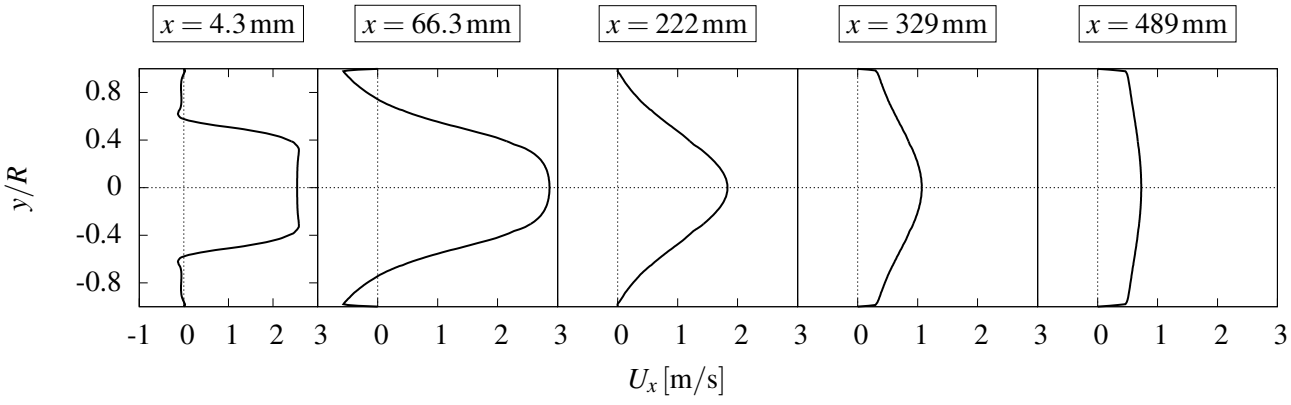


**Figure 6.** Velocity profiles in characteristical cross-sections after the orifice.

These transformations of mean axial velocity in axial direction are balanced with changes of mean radial velocity in radial direction, which directly follows from continuity equation (2). In this case, circumferential velocity component is practically negligible in comparison to radial and axial velocity component. This three dimensional velocity field in cross-sections after the orifice also affects the non-uniform pressure field in these cross-sections.

## 6. Conclusion

Numerical calculations of turbulent flow of water through orifice flow meter with RANS modeling approach is performed in the research presented in this paper. It is shown that for this types of turbulent flow standard $k$-$\varepsilon$ model gives very good agreement to experimental results for pressure drop. It is also shown that numerical mesh generated with snappyHexMesh utility can also be used for computations in terms of good accuracy of results for global physical quantities. Detailed analysis of the results in region near the orifice revealed existence of two different vortex structures - large primary vortex as a consequence of sudden area expansion after the orifice, and small secondary vortex in the corner region between orifice and pipe wall.

**Acknowledgement.** This work is supported by the Ministry of Education, Science and Technological Development, Republic of Serbia through project TR 35046.

## References

[1] Durst, F., Wang, A.B., *Experimental and numerical investigation of the axisymmetric, turbulent pipe flow over a wall-mounted thin obstacle*. In: Seventh Symposium on Turbulent Shear Flows, Stanford University, 21-23, 1989

[2] Ćoćić A.S., Lečić M.R., Čantrak S.M., *Investigation of Structure of Turbulent Flow in Circular Pipe With Sudden Area Contraction by Use of Invariant Theory and Numerical Simulations*, In Proceedings of 14th International Conference of Modelling Fluid Flow (CMFF 09), 2009

[3] ERCOFTAC Classical Database, http://cfd.mace.manchester.ac.uk/ercoftac/

[4] Lumley, J.L., Newmann, G. *The return to isotropy of homogeneous turbulence*, Journal of Fluid Mechanics, Vol. 82, 161-178, 1978.

[5] Smith, E., Ridluan, A., Somravysin, P., Promvonge, P., *Numerical investigation of turbulent flow through a circular orifice*, KMITL Science and Technology Journal, Vol. 8, 43-50, 2008.

[6] Roul, M.K., Sukanta, D.K., *Single-Phase and Two-Phase Flow Through Thin and Thick Orifices in Horizontal Pipes*, Journal of Fluids Engineering, Vol. 134, 091301:1-14, 2012.

[7] Manish S.S., Jyeshtharaj, B.J., Kalsi, A.S., Prasad, C.S.R., Shukla D.S., *Analysis of flow through an orifice meter: CFD simulation*, Chemical Engineering Science, Vol. 71, 300-309, 2012

[8] Nygård, F., Andersson, H.I., *Numerical simulations of turbulent pipe flow through an abrupt axisymmetric constriction*, Flow Turbulence Combustion, Vol. 91, 1-18, 2013.

[9] Weller, H.G., Tabor G., Jasak, H. and Fureby, C., *A Tensorial Approach to CFD using Object Orientated Techniques*, Computers in Physics, Vol. 12 No. 6, 620 - 631, 1998.

[10] Jones, W. P. and Launder, B. E., *The prediction of laminarization with a two-equation model of turbulence*. International Journal of Heat and Mass Transfer, Vol 15, 301âĂŞ314, 1972

[11] Launder, B. E. and Sharma, B. I., *Application of the Energy-Dissipation Model of Turbulence to the Calculation of Flow Near a Spinning Disc*, Letters in Heat and Mass Transfer, Vol. 1, No. 2, 131-138, 1974.

[12] Wilcox, D.C., *Re-assessment of the scale-determining equation for advanced turbulence models* , AIAA Journal, Vol. 26, No. 11, 1299-1310, 1988.

[13] OpenFOAM User Guide, 2016, http://www.openfoam.com/docs/

[14] Raković, M.M., *Numerical calculations of turbulent flow of water through the pipe with orifice flow meter*, MSc Thesis (in Serbian), University of Belgrade, Faculty of Mechanical Engineering, 2016.

[15] Warming, R., Beam, R. *Upwind second order differencing schemes and applications in aerodynamic flows*, AIAA Journal, Vol. 14, 1241-1249, 1976.

[16] Ferziger J.H., Perić, *Computational Methods for Fluid Dynamics*, 3rd Edition, Springer, 2002.

[17] Patankar S.V. and Spalding D. B., *A Calculation Procedure for Heat, Mass and Momentum Transfer in 3-Dimensional Parabolic Flows*, Int. J. Heat Mass Transfer, Vol. 15, 1787-1806, 1972.